Article:
Gavriloaea, Paul Iulian, Ross, Jackson L., Freimuth, Frank et al. (5 more authors) (2025) Efficient motion of 90° domain walls in Mn2Au via pure optical torques. npj Spintronics. 11. ISSN: 2948-2119

https://doi.org/10.1038/s44306-025-00075-2

https://doi.org/10.1038/s44306-025-00075-2

Efficient motion of 90° domain walls in Mn_2Au via pure optical torques

Paul-Iulian Gavriloaea [1] ✉, Jackson L. Ross [2], Frank Freimuth [3,4], Yuriy Mokrousov [3,4], Richard F. L. Evans [2], Roy Chantrell [2], Oksana Chubykalo-Fesenko [1] & Rubén M. Otxoa [5,6] ✉

Discovering alternative ways to drive domain wall (DW) dynamics is crucial for advancing spintronic applications. Here we demonstrate via atomistic spin dynamics simulations that a novel laser optical torque (LOT) excited in the visible spectrum can efficiently drive 90° DWs in the Mn_2Au antiferromagnet but its spatial symmetry forbids the motion of 180° walls. In the steady-state regime, the kinematics display special relativity signatures accessed for low laser intensities. At velocities higher than the magnonic limit, the DW enters a proliferation regime in which part of its relativistic energy is invested into the nucleation of novel magnetic textures. The unique LOT symmetry allows the precise control of the DW motion direction rotating the laser polarisation or tailoring the wall chirality. Our investigation contributes towards the fundamental understanding of opto-magnetic effects, supporting the development of next-generation, all-optically controlled antiferromagnetic spintronics.

Antiferromagnets (AFMs) are envisioned as promising active elements for the next generation of spintronic devices[1,2]. To this end, rapid and efficient manipulation of magnetic domain walls (DWs) is desired, aiming towards the realisation of race-track memories[3,4], logic architectures[5–7] or unconventional computing protocols[8–10]. In ferromagnets (FMs), DW velocities are significantly hindered by internal instabilities known as the Walker breakdown[11–13] or by spin-wave (SW) emission analogous to the Cherenkov effect[14,15]. AFMs however, can display relativistic DW kinematics limited only by the maximum group velocity of the medium, typically of the order of tens of km/s[16,17].

The state-of-the-art mechanism employed to manipulate the AFM order relies on the relativistic, current-induced Néel Spin-Orbit Torque (NSOT) effect[18] shown to induce switching[19–23] and DW motion[16,17,24,25]. At the same time, laser pulse excitation displays the fastest and least dissipative control of the magnetic order observed so far[26]. Several studies addressed the question of light-matter interaction in AFMs[7,27–33], with THz laser pulse excitation shown recently capable of driving ultra-fast, non-linear dynamics in Mn_2Au via NSOT[34]. However, the experimental demonstration of all-optical AFM DW dynamics is yet to be achieved.

A recent ab initio investigation concerning the symmetry and magnitude of the laser-induced magnetic response in the layered AFM Mn_2Au[35,36] revealed the appearance of a substantial torque on the Néel order parameter $\boldsymbol{l}$ of tens of mT, as a result of visible light excitation, thus far above the THz regime typically employed experimentally. Within the non-equilibrium Keldysh formalism[35,37], a linearly or circularly polarised laser pulse excitation at optical frequencies was shown to excite such a torque through the appearance of a staggered opto-magnetic field which couples to the Mn spins in the distinct AFM sublattices. To distinguish this effect from the previously studied NSOT, we will hereon employ laser optical torque (LOT) terminology. The physical origin of this effect is being attributed collectively to the Optical Spin Transfer Torque[38,39] and the Inverse Faraday Effect[40,41]. The NSOT effect scales linearly with the laser electric field $\boldsymbol{E}$ and is dominant at THz frequencies. Since this first-order response oscillates with the frequency ω of the laser field, in the visible frequency spectrum the NSOT cannot excite the Mn_2Au AFM due to the large mismatch between ω and the AFM resonant frequencies. In contrast, the LOT is a second-order response which scales quadratically with $\boldsymbol{E}$. The dc contribution of this second-order response makes LOT dominant at optical frequencies[35,37]. Recently, this LOT mechanism was predicted capable of inducing coherent 90° and 180° switching of the AFM order parameter on the ultra-fast timescale[42]. Importantly, the symmetry of the LOT effect is radically distinct from NSOT which in ref. 42 is shown to give rise to toggle switching by means of the same laser polarisation, in contrast with conventional NSOT where the polarity of the $\boldsymbol{E}$-field must be flipped (be it with current or THz excitation)[20,21,34]. It is thus fundamentally interesting to apply the little-explored LOT mechanism also in the problem of DW dynamics.

[1]Instituto de Ciencia de Materiales de Madrid, CSIC, Cantoblanco, 28049 Madrid, Spain. [2]School of Physics, Engineering and Technology, University of York, YO10 5DD York, UK. [3]Institute of Physics, Johannes Gutenberg University Mainz, 55099 Mainz, Germany. [4]Peter Grünberg Institut and Institute for Advanced Simulation, Forschungszentrum Jülich and JARA, 52425 Jülich, Germany. [5]Hitachi Cambridge Laboratory, CB3 0HE Cambridge, UK. [6]Donostia International Physics Center, 20018 Donostia San Sebastian, Spain. ✉e-mail: paul.gavriloaea@csic.es; ro274@cam.ac.uk

Here, we combine the ab initio results in ref. 35 with atomistic spin dynamics (ASD) simulations[43], in an investigation of optically driven DW kinematics in Mn_2Au. Depending on the relative orientation between the Néel vector $\boldsymbol{l}$ and the electrical field component $\boldsymbol{E}$ of the applied laser pulse, the symmetry and magnitude of the induced optical torque can be established. We demonstrate that the LOT mechanism predicted in ref. 35 may drive 90° DW dynamics. Interestingly, its symmetry does not allow the motion of 180° DWs, in contrast with the NSOT mechanism[16,17,24,25]. Our numerical study is complemented by a theoretical, two-sublattice σ-model[16,44–48], adapted for the present case. Finally, we describe the activation of highly non-linear AFM DW dynamics in the supermagnonic regime accompanied by spontaneous DW proliferation events. The last section of the manuscript is devoted to discussion and perspectives of the developed ASD model.

Results

Mn_2Au is a layered, collinear AFM with four magnetic sublattices in the unit cell (see sketch in Fig. 1) and is characterised by the so-called PT-symmetry[18]. Inside each layer, Mn atoms are ferromagnetically coupled. This material possesses a complex set of anisotropies with cubic and uniaxial in-plane as well as uniaxial out-of-plane components (see "Methods" section). Thus, in principle, both 180° and 90° in-plane DWs are possible in Mn_2Au, although experimentally, when grown in a thin film form, mostly 90° domains have been reported[32,34,49]. The special PT-symmetry ensures the existence of intrinsic NSOT which can efficiently move 180° DWs in Mn_2Au by applying electric current[16,17,24].

Here by means of large-scale ASD modelling, we investigate DW dynamics driven by LOT. For this purpose, we numerically integrate the set of coupled Landau-Lifshitz-Gilbert (LLG) equations for localised atomic magnetic moments in a 7 μm long Mn_2Au track. Importantly, Mn_2Au with its material parameters such as anisotropy and exchange in addition to the LOT magnitude have been obtained previously via ab initio calculations[35,50,51]. In the "Atomistic spin dynamics" section, we give details on the ASD model of Mn_2Au and the material constants.

According to[35], a linearly polarised pulse at visible frequency, propagating with $\boldsymbol{k}||Oz$ (perpendicular to the Mn planes) and with the electric field $\boldsymbol{E}$ set parallel to the [110] direction with respect to the Mn_2Au unit cell (see Fig. 1a), leads to the appearance of a LOT ($\boldsymbol{T}^{\boldsymbol{l}}_{\mathrm{opt}}$) canting the Néel vector $\boldsymbol{l}$ in the Oz direction as described by tensor 24 in Table I of ref. 35 (also consult Table 1 in the present work). According to spatial symmetry arguments (see the "LOT analysis: from ab initio to atomistic spin dynamic" section for details), the induced LOT depends on the local orientation of the Néel vector and the $\boldsymbol{E}$-field as:

$$\boldsymbol{T}^{\boldsymbol{l}}_{\mathrm{opt}} = A\cos(2\varphi)\sin(2\psi)\hat{\boldsymbol{z}}, \tag{1}$$

where A is the torque amplitude (scaled linearly with the laser intensity, see "Methods" section), φ and ψ measure the azimuthal deviation of $\boldsymbol{l}$ and $\boldsymbol{E}$ with respect to Ox which coincides with the [100] crystalographic direction (Fig. 1a). To maximise the optical torque magnitude we consider here $\psi = 45°$. Crucially, the NSOT has the symmetry of Zeeman torque (i.e., proportional to $\cos(\varphi)$ when the current is applied parallel to the [100] direction)[16,17] and thus radically distinct compared to the LOT mechanism described here. Particularly, as it will be detailed later, the $\cos(2\varphi)$ symmetry of the LOT leads to displacement of 90° DWs and impedes the motion of 180° walls. The LOT corresponds to a staggered opto-magnetic field $\boldsymbol{H}^{i}_{\mathrm{opt}}$, which we couple to the local spin $\mathbf{S}_i$ in our ASD model (see "Atomistic spin dynamics" section for the complete Hamiltonian) via the relationship:

$$\boldsymbol{H}^{i}_{\mathrm{opt}} = \frac{1}{\mu_0}\boldsymbol{T}^{\boldsymbol{l}}_{\mathrm{opt}} \times \mathbf{S}_i. \tag{2}$$

In Fig. 1b we schematically represent the top view of the 90° DW in the track at a time t during the laser excitation. Focusing on the DW centre, i.e., on the atomic site where $\boldsymbol{l}$ lies parallel to Ox ($\varphi = 0$), we appreciate that the LOT ($\boldsymbol{T}^{\boldsymbol{l}}_{\mathrm{opt}}$) cants the sublattices $\mathbf{S}_A$, $\mathbf{S}_B$ towards Oz, as graphically detailed in Fig. 1(c). Under the strong AFM coupling, local exchange fields $\boldsymbol{H}^{A}_{e}$, $\boldsymbol{H}^{B}_{e}$ torque the bipartite system such that the Néel vector rotates counter-clockwise in the Oxy plane, driving the 90° DW in the subsequent time step $t + \Delta t$ towards $+Ox$, as seen in Fig. 1(d) and (e).

At the same time, the $\cos(2\varphi)$ spatial variation of $\boldsymbol{T}^{l}_{\mathrm{opt}}$ hinders the dynamics of an 180° DW. The key factor which enables the 90° displacement with LOT is that it acts along the same direction (parallel or antiparallel to Oz) at all the atomic sites within the boundaries of the wall such that a preferential DW sense of motion can be established. This resembles the NSOT-driven dynamics in the 180° DW geometry[16,17]: the NSOT symmetry — with the torque proportional to $\cos(\varphi)$— leads to zero torque at the boundaries of the 180° configuration and preserves the same sign torque across the transition region between domains. Contrarily, LOT changes sign twice in a 180° geometry such that the boundaries (green shaded) and the wall region (purple shaded) tend to rotate in opposite directions (clockwise

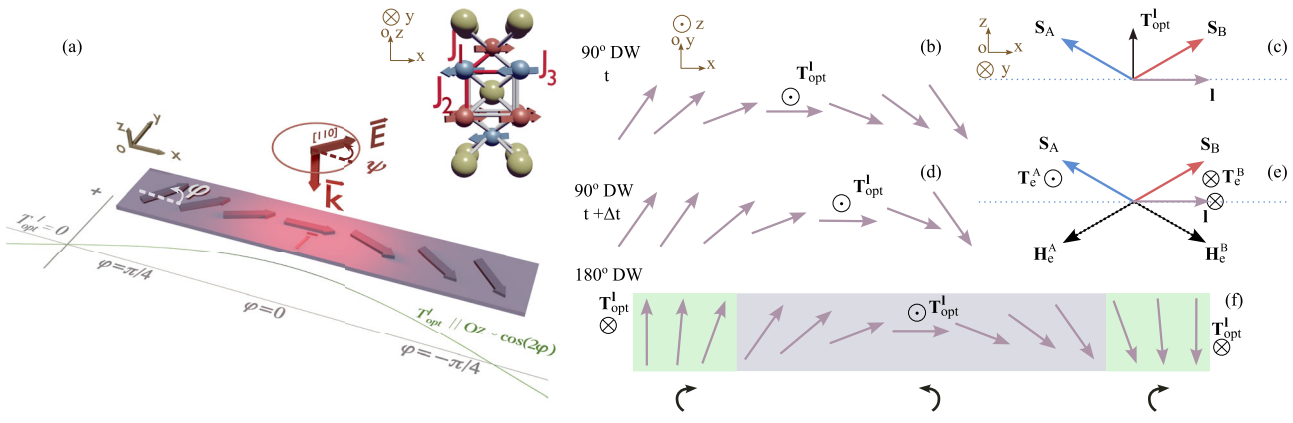

Fig. 1 | All-optical 90° DW dynamics in Mn_2Au. a A laser pulse in the optical spectrum propagating with $\boldsymbol{k}||Oz$, and with $\boldsymbol{E}$ polarised along the [110] diagonal ($\psi = 45°$), will lead to an OOP torque determined by the local spin orientation and proportional to the laser intensity[35]. The angles φ and ψ are defined with respect to the Ox axis. In the top right corner, we represent the geometry of the unit cell along with the J_1, J_2 and J_3 exchange interactions. In red and blue we colour the Mn atoms in the staggered sublattices while the Au atoms are represented in gold. **b** At a time t, the optical torque gives rise to an OOP canting of the sublattices $\mathbf{S}_A$, $\mathbf{S}_B$ seen in (**c**). Large exchange fields $\boldsymbol{H}^{A}_{e}$, $\boldsymbol{H}^{B}_{e}$ torque the bipartite system such that the Néel vector rotates counter-clockwise in the Oxy plane, promoting the displacement of the 90° DW in the subsequent time step $t + \Delta t$ (**d**, **e**). 180° DW motion under the same optical torque symmetry is not allowed (**f**).

Table 1 | Allowed LOT symmetries in Mn_2Au for an in-plane Néel vector geometry as calculated in ref. 35

ID in ref. 35	χ_{ijkpq} given in ref. 35	$T_i \propto \chi_{ijkpq}$	$T_i \propto \varphi, \psi$
3	⟨23212⟩ − ⟨13121⟩	$T_{yx} \propto \epsilon_z \epsilon_y^* l_x l_y - \epsilon_z \epsilon_x^* l_y l_x$	$T_{yx} = 0\ (\epsilon_z = 0)$
4	⟨32221⟩ − ⟨31112⟩	$T_z \propto \epsilon_y \epsilon_y^* l_y l_x - \epsilon_x \epsilon_x^* l_x l_y$	$T_z \propto -\sin(2\varphi)\cos(2\psi)$
9	⟨21311⟩ − ⟨12322⟩	$T_{yx} \propto \epsilon_x \epsilon_z^* l_x l_x - \epsilon_y \epsilon_z^* l_y l_y$	$T_{yx} = 0\ (\epsilon_{zz^*} = 0)$
24	⟨31211⟩ − ⟨32122⟩	$T_z \propto \epsilon_x \epsilon_y^* l_x l_x - \epsilon_y \epsilon_x^* l_y l_y$	$T_z \propto \cos(2\varphi)\sin(2\psi)$

The table discusses the link between the angular-dependent expressions of the LOT used throughout this work and the original tensorial notation.

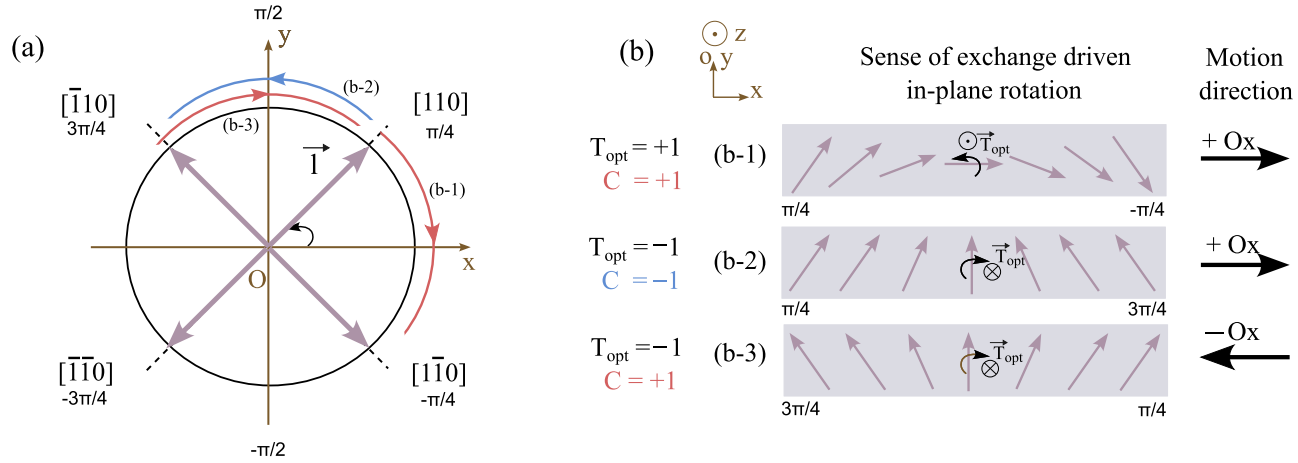

Fig. 2 | Analysis of DW motion direction with respect to DW chirality. a Mapping the in-plane Néel vector orientation in the magnetic track along the unit circle. We display the four possible 90° DW boundaries corresponding to the $K_{4||}$ easy directions. Taking as reference the Néel vector parallel to the [110] diagonal, we can obtain two DW geometries with right and left-hand-side chirality (the sense of rotation and the colours of the red/blue arrows in (**a**) represent the right/left-hand-side chirality) labelled (b-1) and (b-2) respectively. The corresponding spin configurations are displayed in subplot (**b**). ASD spin dynamics simulations reveal these two DWs displace in the same direction + *Ox* because the handedness of the in-plane Néel vector rotation opposes the chirality of the wall in both cases. Distinctly, the (b-3) wall geometry is driven towards − *Ox* because the in-plane spin reorientation matches the chirality of the wall.

and counter-clockwise, respectively) leading to an expansion/contraction of the DW texture but no overall displacement, see Fig. 1f. Direct ASD simulations have confirmed that 90° DWs are efficiently moved by LOT and that 180° DWs under its action only contract or expand.

Note additionally that there is another out-of-plane (OOP) LOT symmetry, labelled tensor 4 in ref. 35, which is predicted to arise for light polarised either along *Ox* or *Oy*, given an in-plane Néel vector (see Table 1). This term is proportional to $-\sin(2\varphi)\cos(2\psi)$, which changes sign across the 90° wall due to the $\sin(2\varphi)$ angular variation and thus cannot move it. Additionally, for $\psi = 45°$ which corresponds to the laser geometry in Fig. 1, this contribution is zero. At the same time, the combined effect of tensors 4 and 24 can efficiently switch the AFM domains[42]. The two other in-plane LOT symmetries labelled 3 and 9 in ref. 35, arise for ***E*** polarised in the *Oxz* or *Oyz* planes. However, these torques cannot efficiently move DWs due to the large $K_{2\perp}$ anisotropy which competes against the canting of the individual sublattices in the *Oxy* plane. Moreover, in our ***E***-field geometry, these contributions are shown to be zero as discussed in the "Methods" section.

The DW motion direction depends on the product of DW chirality and the LOT direction (Fig. 2). Mapping the spin configuration along the unit circle, one can trace eight possible 90° DW geometries in our bi-axial AFM. ASD simulations reveal four of these configurations will displace along + *Ox* while the other four in the opposite − *Ox* direction. The direction of motion depends on the sign of the optical torque relative to the chirality of the wall. We assign $C = +1$ for right-hand-side DW chirality (clockwise spin rotation) and $C = -1$ for left-hand-side DW chirality (counter-clockwise spin rotation). Since the optical torque maintains its sign across the DW configuration, we can distinguish two situations, positive and negative optical torque $T_{opt} = \pm 1$. If the product $T_{opt}C$ is positive, the DW will displace towards + *Ox*, otherwise, the motion will take place in the opposite direction. In Fig. 2 we exemplify this behaviour for three distinct DW configurations. Taking as a reference the Néel vector parallel to the [110] direction in Fig. 2a, we construct two 90° DW configurations following a right or left-hand-side rotation along the unit circle. The corresponding spin arrangements labelled (b-1) and (b-2) can be observed in Fig. 2b. Both T_{opt} and C change their sign in between the two geometries, hence the product $T_{opt}C$ remains positive and the DW displacement direction is preserved. This can be understood in light of the strong in-plane AFM torque excited in the two-step driving mechanism discussed in Fig. 1. Depending on the sign of T_{opt}, the resulting in-plane rotation of the Néel vector will take place in opposite directions. $T_{opt} = +1$ gives rise to counter-clockwise rotation, while $T_{opt} = -1$ promotes clockwise rotation. To maintain the DW direction of motion, the handedness of this in-plane rotation must oppose the chirality of the wall. Therefore the T_{opt} change of sign in between configurations (b-1) and (b-2) matches this requirement and thus preserves the direction of motion towards + *Ox*. The situation changes if we compare the (b-2) and (b-3) 90° DW profiles. Here the $T_{opt}C$ product changes sign which promotes displacement in opposite directions as confirmed by our ASD simulations. Taking as a reference any other 90° DW configuration along the unit circle in Fig. 2a, we observe the same behaviour.

It is also worth pointing out here that a 90° rotation of the ***E***-vector to the $[1\bar{1}0]$ ($\psi = -45°$) direction changes the sign of the LOT and consequently the direction of motion. In turn, a 180° rotation to $[\bar{1}\bar{1}0]$ ($\psi = -135°$) preserves the positive sign of the torque and the motion direction towards + *Ox* given $C = +1$.

Our direct ASD simulations show that 90° DWs propagate along the track under the action of LOT as dynamical solitons, i.e., with a stationary velocity and no change in shape until the driving force reaches some threshold value, see Fig. 3. A well-known behaviour of AFM solitons, mainly discussed previously for 180° DWs[16,17], the laser-induced dynamics of our

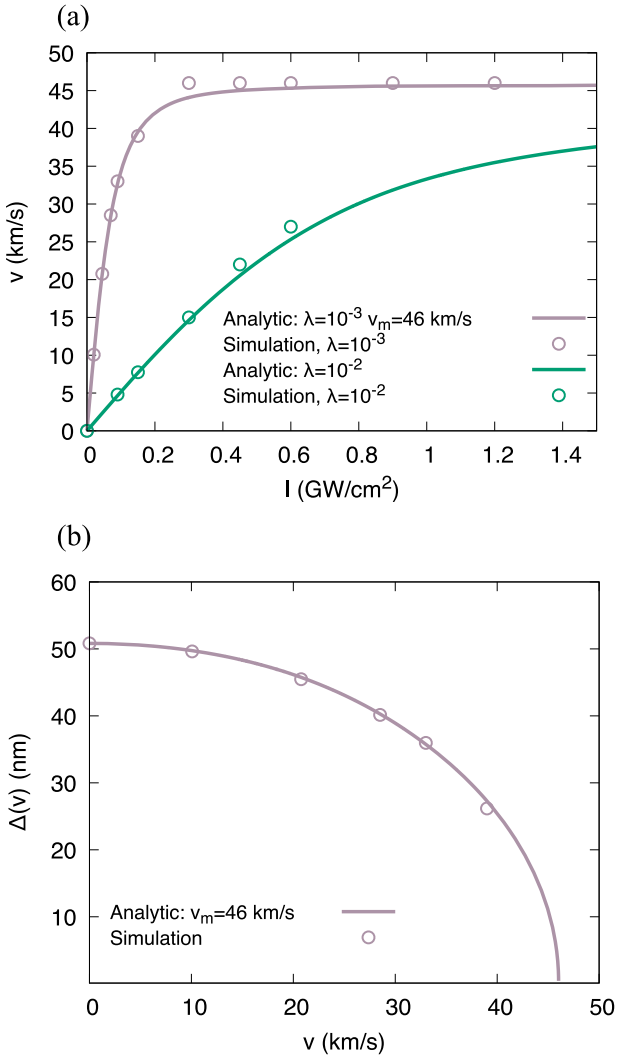

Fig. 3 | Numerical results and SG predictions of steady-state 90° DW dynamics. **a** Velocity saturation with the laser intensity for $\lambda = 10^{-2}$ and $\lambda = 10^{-3}$. **b** Contraction of the DW width as a function of the propagation velocity. Theory and calculations yield the same wall width at rest (up to two decimals): $\Delta_0 = 50.82$ nm. The numerical results overestimate the maximum velocity to a value of 46 km/s compared to the analytical prediction of 43.39 km/s. For better fitting, we adjust v_m to the former value in subplots (**a**) and (**b**).

90° wall display special relativity signatures manifesting through wall-width contraction as the propagation velocity approaches the "magnonic barrier" — see Fig. 3. This is revealed in the ASD simulations by applying a constant, laser-induced torque of increasing strengths which allows us to access a steady-state DW motion regime.

The numerical results compare well with analytical predictions obtained within a two-sublattice, σ non-linear model which maps the AFM LLG equations of motion expressed for the $\boldsymbol{l}$ and $\boldsymbol{n}$ vectors onto a Lorentz-invariant, sine-Gordon (SG) like equation[16,44–48] in terms of the azimuthal angle φ. Here we adapt this model for 90° DWs and LOT (see Supplemental Material section I). For ease of calculation in the analytical model presented here, we perform a 45° in-plane rotation of the $K_{4||}$ easy-axes such that they point along the Ox and Oy cartesian directions in contrast with Fig. 1. For this reason, the angular variation of the optical torque acting on the Néel vector $\boldsymbol{l}$ is $\propto \sin(2\varphi)$. The SG-like equation thus reads:

$$\partial_x^2\varphi - \frac{1}{v_m^2}\ddot{\varphi} - \frac{1}{4\Delta_0^2}\sin 4\varphi - h_{opt}\sin(2\varphi) - \eta\dot{\varphi} = 0, \qquad (3)$$

where v_m is the effective "speed of light" or the magnonic limit, encoded by the exchange interactions and evaluated in our case to $v_m = \sqrt{a|J_1|}/\hbar = 43.39$ km/s, where $a = 8a_0^2(J_3 + |J_1|/2)$ and a_0 is the spin-lattice constant along Ox and Oy[48] (see Supplemental Material section I). Importantly, one should note that the role of the AFM parameter J_2 is to keep the sublattices in a weakly non-collinear AFM state. Once this state is ensured, the dynamics are independent on J_2, as previously demonstrated in ref. 48. Furthermore, $\Delta_0 = \sqrt{a/(8K_{4||})} = 50.8$ nm is the DW width at rest and the reduced optical field h_{opt} is defined as $h_{opt} = 8\gamma\hbar H_{opt}/a$. The last term represents the phenomenological damping field $\eta = 8\lambda\hbar/a$.

In a steady-state motion regime, when the optical excitation counterbalances the dissipation, Eq. (3) admits the soliton solution for the 90° DW profile: $\varphi(x,t) = \arctan[\exp((x - vt)/\Delta(v))]$. The equilibrium between the damping and the optical excitation ensures the steady-state dynamics in (3) and yields the velocity-dependent wall width $\Delta(v) = \Delta_0\sqrt{1 - \frac{v^2}{v_m^2}}$, obeying the Lorentz transformation. Here v is the steady-state velocity $v = \frac{v_m}{\sqrt{1+(v_m/v_0)^2}}$, where $v_0 = 2h_{opt}\Delta_0/\eta$.

In Fig. 3, we analyse the numerical wall width and velocity in the steady-state regime at different laser pulse intensities and compare them with the analytic expressions presented earlier. The simulations compare well with the developed theory (see Supplemental Material section I), below the predicted magnonic barrier.

LOT-excited 90° DW dynamics enter a highly non-linear regime near the magnonic barrier, similar to AFM DW motion driven by NSOT[17]. It is characterised by the proliferation of additional magnetic textures, breaking of the Lorentz invariance and supermagnonic motion, see Fig. 4. Since the LOT "Zeeman-like" energy ($\mathbf{S}_i \cdot \boldsymbol{H}^i_{opt}$) always remains zero in our case, as the geometry in Eq. (2) maintains $\boldsymbol{H}^i_{opt}$ always perpendicular to the local spin direction $\mathbf{S}_i$ (note that the torque is not zero), the question is, therefore, where does the energy required for the nucleation of additional magnetisation textures arise from? In Fig. 4a, we represent the azimuthal angle φ along the track during a 90° wall displacement excited via a half-Gaussian, laser pulse of peak intensity $I = 0.65$ GW/cm^2 (see laser profile in subplot c). Time-steps t_1, t_2, and t_3 show the characteristic low-frequency SW, lagging behind and broadening the width of the 90° DW as it is pushed beyond the magnonic barrier. A gradual, corresponding decrease in the exchange energy is evidenced by Fig. 4b. Due to the competition between the anisotropy and exchange energies, this broadening cannot indefinitely take place, forcing a rebound process characterised by a contraction of the wall. A drastic reduction of the DW width can be observed between t_3 and t_4 along with a large increase in the exchange energy. This continuous deformation leads to the appearance of oscillatory patterns at the front of the propagating wall, which on a ps timescale invest part of the relativistic energy carried by the DW towards the nucleation of an additional magnetisation texture, as evidenced at t_4 and t_5. Unlike the 180° NSOT-driven DW case[17], the newly formed pattern does not follow the geometry of the parent texture as further evidenced by Fig. 4d, e. Visible at t_6, t_7 and t_8, the initial spin structure morphs into a static magnetisation texture pinned around the $x = 3.5$ μm mark, while its surplus, relativistic energy is invested towards pushing ahead a novel spin structure. The pair spin textures are stable in a reasonable timeframe achieved by atomistic simulations after the laser pulse is stopped and provided they do not overlap.

The physical origin of the effect relies on the rapid transfer of relativistic energy from a propagating DW near the magnonic barrier into new stable magnetisation textures. Comparing snapshots t_3 and t_5, we estimate the energy transfer across the track from the parent to the child magnetic texture takes place with an average velocity of 89 km/s (0.89 μm travelled in 10 ps), largely exceeding the speed limit of a steady-state soliton, also called the "effective speed of light". This breakdown of the Lorentz invariance and soliton-like behaviour occurs due to dynamical changes of the DW shape which result in the creation of new textures with repulsive interaction leading to acceleration. Interestingly, these results can find similarities with dislocation dynamics. As shown in refs. 52,53, dislocations may enter a

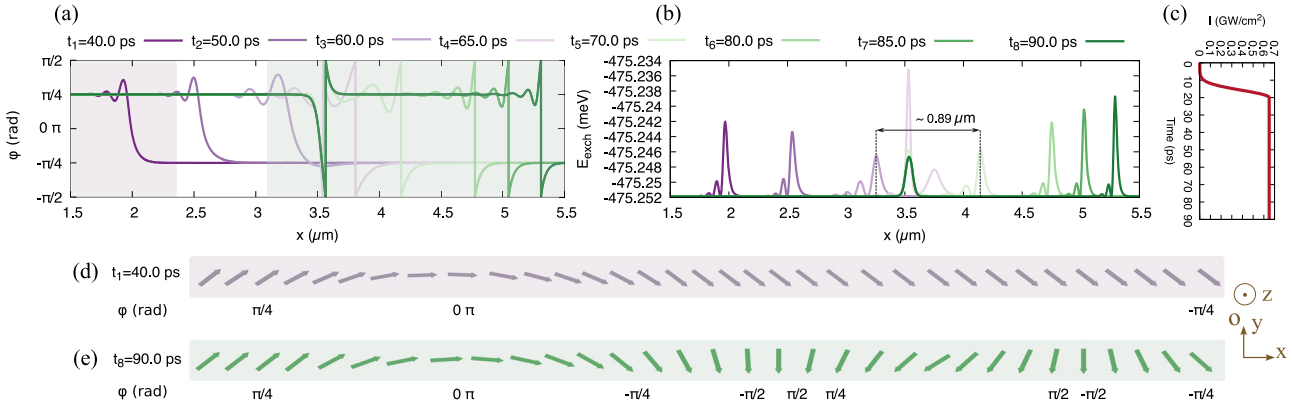

Fig. 4 | Proliferation event in the supermagnonic regime. a $\varphi(x, t)$ variation along the track during the 90° DW displacement. Time snapshots t_1, t_2 and t_3 showcase a gradual wall-width broadening and a corresponding decrease in the exchange energy penalty E_{exch} (**b**) under the influence of the lagging SW mode. A subsequent rebound contraction and increase of E_{exch} takes place due to the competition between the exchange and anisotropy energies, leading to oscillatory patterns at the front of the propagating wall, which result into a proliferation event seen at t_4 and t_5. The initially moving DW morphs into a static magnetic pattern pinned around the $x = 3.5$ μm mark, while the surplus relativistic energy is invested towards pushing ahead the novel spin structure. The energy transfer from the parent to the child magnetic texture takes place with an average velocity of ≈89 km/s, extracted by comparing snapshots t_3 and t_5. Subplots (**a**) and (**b**) share the time legend. **c** Optical excitation protocol with a peak laser intensity of $I = 0.65$ GW/cm^2. **d**, **e** Schematics of the Néel vector configuration corresponding to the purple and green shaded regions in (**a**), at $t_1 = 40$ ps and $t_8 = 90$ ps respectively.

super-sonic regime surpassing the sonic barrier, the underlying reason for this being the generation of secondary kinks (topological defects) via the so-called "mother-daughter" kink nucleation.

Finally, we would like to point out another interesting effect obtained under a rotation of the ***E***-field laser polarisation vector. So far, the effect of LOT was calculated with the assumption that the ψ azimuthal angle is 45°, or in other words the electric field ***E*** was aligned parallel to the [110] direction. Interestingly, rotating the ψ angle to 0° or 90° which corresponds to ***E*** || [100] and ***E*** || [010] respectively, leads to periodic DW contraction and expansion on the ultra-fast timescale (in these geometries, the LOT symmetry is given by tensor 4 which is maximal in amplitude while tensor 24 is zero as seen in Table 1). In Fig. 5 we display the time variation of the DW width as a function of increasing laser pulse intensity for the two distinct ***E***-field geometries demonstrating periodic contraction and expansion of the wall on the ultra-fast timescale. Notably, the amplitude of the oscillations is proportional to the laser pulse intensity and the time-dependent signal is dephased in between the two laser polarisations leading first to expansion followed by contraction in the $\psi = 0°$ case whilst the situation is reversed at $\psi = 90°$. Since the exchange contributions to the total energy of the DW are prevalent over their anisotropic counterparts, naturally the expansion processes of the wall are enhanced in amplitude compared to the observed contraction.

Discussion

Our simulations revealed the possibility of driving a 90° AFM DW under the novel LOT mechanism. Interestingly, unlike the NSOT mechanism, this excitation protocol does not allow the motion of 180° DWs. Typical experiments of laser-induced DW dynamics in FMs make use of fluences in the range of a few mJ/cm^2 which amount to intensities normally in the 1 and 10 GW/cm^2 interval[41,54]. In comparison, we predict 90° DW kinematics up to the supermagnonic limit ($v = 46$ km/s) by single pulse excitation below 0.3 GW/cm^2. Although heating effects are expected due to the metallic nature of Mn_2Au, we estimate via a two-temperature model the ultra-fast picosecond phonon heating timescale with temperature going back to room one at a timescale below 1 ns (see Supplemental Material section II). A particularly important advantage of LOT compared to the NSOT mechanism is its reliance on laser excitations in the visible spectrum routinely excited in ultra-fast experiments in contrast with the much more challenging THz setups.

In addition to the possibility for all-optical 90° DW dynamics, the LOT mechanism offers abundant rich physics and potentially interesting features for device applications. We systematically characterised the role of the DW chirality in setting the motion direction as well as analysed the effect of rotating the ***E***-field polarisation vector. Interestingly, by adjusting the ***E*** orientation we can also achieve a pinned AFM DW configuration whilst periodically driving width contraction and expansion on the ultra-fast timescale displaying thus a route to explore potential applications for AFM domain wall-based nano-oscillators[55,56].

Manipulating highly non-linear dynamics in magnetic systems may play an important role in the development of future neuromorphic reservoir computing archetypes[10,57,58]. We envision thus a combined, opto-electronic experimental scheme, towards the realisation of a multiple-node reservoir. Driven by an optical input, fast and periodic nucleation events could be manipulated in an AFM DW fabric[59], whereas based on the anisotropic magnetoresistive effect[21], an output electrical signal may be correlated to changes in the magnetic texture, thus posing an interest for pattern recognition and prediction applications.

Evidently, in experiments, the DW dynamics may be influenced by the presence of defects, magnetostriction effects, multi-domain states etc and all pose interesting fundamental questions which deserve to be analysed. A particularly interesting question is the influence of acoustic waves and the spin-phonon coupling on the DW velocity. Previously, in orthoferrites crystals, certain velocity anomalies with respect to the strength of the excitation were attributed to magnetoelastic contributions[60]. Lastly, the diversity and natural abundance of antiferromagnetically ordered materials call for an exploration of similar optical torque symmetries in other crystal structures, as well as the natural extension towards the emergent landscape of altermagnets[61].

Methods

Atomistic spin dynamics

The extended Heisenberg Hamiltonian in our Mn_2Au system is[17,20,48]:

$$\begin{aligned}\mathcal{H} \;=\; & -\sum_{\langle i,j\rangle} J_{ij}\mathbf{S}_i\cdot\mathbf{S}_j - K_{2\perp}\sum_i (\mathbf{S}_i\cdot\boldsymbol{z})^2 - \tfrac{K_{4\perp}}{2}\sum_i (\mathbf{S}_i\cdot\boldsymbol{z})^4 \\ & -\tfrac{K_{4\parallel}}{2}\sum_i\left[(\mathbf{S}_i\cdot\boldsymbol{u}_1)^4+(\mathbf{S}_i\cdot\boldsymbol{u}_2)^4\right] - \mu_0\mu_s\sum_i \mathbf{S}_i\cdot\boldsymbol{H}^i_{\text{opt.}}\end{aligned} \tag{4}$$

The adimensional $\mathbf{S}_{i,j}$ unit vectors denote the orientation of the local spin magnetic moments at sites i and j. The first energy term characterises the nearest-neighbours exchange interactions between $\mathbf{S}_i$ and $\mathbf{S}_j$. $J_{ij} = (J_1, J_2, J_3)$ collectively denotes three interactions present within the unit cell, two of AFM kind (J_1, J_2) and a third FM-like exchange (J_3). The Hamiltonian also contains three magnetocrystalline anisotropy

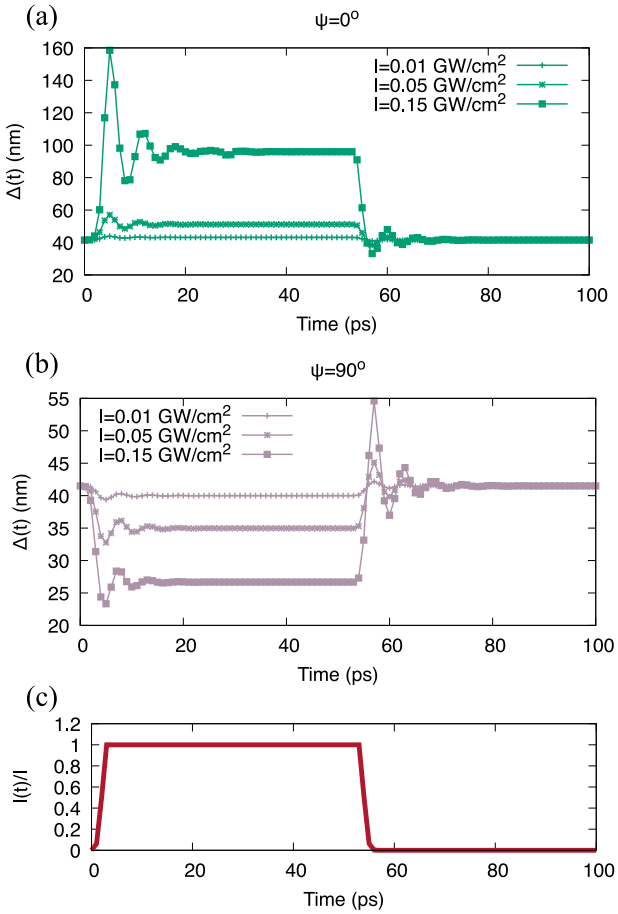

Fig. 5 | Periodic ultra-fast DW contraction and expansion. Subplots (**a**) and (**b**) display the time variation of the DW width for increasing laser pulse intensity with the ***E***-field vector polarised along [100] ($\psi = 0°$) and [010] ($\psi = 90°$) respectively (in these geometries, the LOT symmetry is given by tensor 4 which is maximal in amplitude while tensor 24 is zero as seen in Table 1). We underline the DW in these situations is pinned and no overall displacement along the track is observed. Subplot (**c**) displays the laser intensity as a function of time normalised to the peak intensity. The LOT magnitude is proportional to the laser intensity as discussed in the Methods section.

terms which stabilise an in-plane 90° DW configuration: one easy-plane contribution $K_{2\perp}$ and two tetragonal terms $K_{4\perp}$ and $K_{4||}$. The unit vectors $\boldsymbol{u}_1$, and $\boldsymbol{u}_2$ denote the in-plane, diagonal directions [110] and [1$\bar{1}$0], respectively. We underline in the SG-like equation given in (3), that these easy directions are rotated such that they point along [100] and [010] instead to facilitate the calculations. The last energy term describes the Zeeman interaction with the staggered optical field $\boldsymbol{H}^i_{\rm opt}$, where μ_s is the Mn atomic magnetic moment and μ_0 is the vacuum permeability. The unit-cell geometry used in our work and the material parameters correspond to the previous works in refs. 17,20,48. Thus, the lattice constants in the tetragonal unit cell are set to $a_0 = 3.328$ Å along Ox, Oy and $c = 8.539$ Å on Oz[50]. The atomistic exchange constants evaluate to $J_1 = -5.4673 \times 10^{-21}$ J/link, $J_2 = -7.3451 \times 10^{-21}$ J/link and $J_3 = 1.5877 \times 10^{-21}$ J/link[50]. Further, the anisotropy constants are given by $K_{2\perp} = -1.303 \times 10^{-22}$ J/atom, $K_{4||} = 1.8548 \times 10^{-25}$ J/atom and $K_{4\perp} = 3.7096 \times 10^{-25}$ J/atom[51]. Finally, the Mn atomic magnetic moment is equal to $\mu_s = 3.73\,\mu_B$[35]. For the investigation of DW dynamics, we integrate the LLG equation below:

$$\frac{d\mathbf{S}_i}{dt} = -\frac{\gamma}{1+\lambda^2}\mathbf{S}_i \times \left[\boldsymbol{H}^i_{\rm eff} + \lambda\left(\mathbf{S}_i \times \boldsymbol{H}^i_{\rm eff}\right)\right], \tag{5}$$

where γ is the electron gyromagnetic ratio and λ is an adimensional, phenomenological damping parameter. The effective field acting at each atomic site i given by: $\boldsymbol{H}^i_{\rm eff} = -\frac{1}{\mu_0 \mu_s}\frac{\delta \mathcal{H}}{\delta \mathbf{S}_i}$[43]. Two distinct damping parameters are considered, $\lambda = 10^{-2}$ and $\lambda = 10^{-3}$. The simulated system is 7 μm in length, four Mn wide and four Mn tall, with periodic boundary conditions along Oy and open boundary conditions along Ox and Oz.

LOT analysis: from ab initio to atomistic spin dynamics

Based on the Keldysh non-equilibrium formalism[37], an expression for the LOT in the Mn_2Au crystal was derived in ref. 35:

$$T_i = \frac{r_0^3 I}{c}\left(\frac{\mathcal{E}_{\rm H}}{\hbar\omega}\right)^2 {\rm Im}\sum_{\rm jkpq} \epsilon_{\rm j}\epsilon^*_{\rm k}\chi_{\rm ijkpq} l_{\rm p} l_{\rm q}, \tag{6}$$

where $r_0 = 4\pi\epsilon_0\hbar^2/(me^2)$ is Bohr's radius, c is the velocity of light and ϵ_0 is the vacuum permittivity. Following $I = \epsilon_0 c E_0^2/2$ is the light intensity and $\mathcal{E}_{\rm H} = e^2/(4\pi\epsilon_0 r_0)$ is the Hartree energy. Finally, ϵ_j, ϵ^*_k denote the j, and k Cartesian components of the light polarisation vector and their complex conjugates respectively, while l_p, l_q indicate the Cartesian components of the Néel vector. The tensor components χ_{ijkpq} describe the allowed LOT symmetries in Mn_2Au given its crystallographic point group and the positions of the up/down spins in the unit cell. Table I in ref. 35 (also Table 1 in this work) presents thirty possible torque symmetries for Mn_2Au which according to equation (6) depend both on the orientation of the Néel vector ***l*** as well as the direction of the ***E*** polarisation vector. In spherical coordinates, these vectors can be written as:

$$\boldsymbol{l} \equiv (\sin\theta_{\rm l}\cos\varphi, \sin\theta_{\rm l}\sin\varphi, \cos\theta_{\rm l}), \tag{7}$$

$$\boldsymbol{E} \equiv (\sin\theta_{\rm e}\cos\psi, \sin\theta_{\rm e}\sin\psi, \cos\theta_{\rm e}), \tag{8}$$

where $\theta_{\rm l}$, $\theta_{\rm e}$ are the polar and φ, ψ the azimuthal angles respectively. The large number of allowed χ_{ijkpq} tensors reduces greatly for an in-plane orientation of the Néel vector ($\theta_{\rm l} = \pi/2$), typical for Mn_2Au experimental samples. In ref. 35 these are labelled as tensors 3, 4, 9 and 24. Below we discuss the symmetries of these torques and link the notation employed in ref. 35 with expressions useful for our ASD. To simplify the discussion we assume the laser polarisation is fixed in the Oxy plane ($\theta_e = \pi/2$). Equations (7), and (8) thus can be recast as:

$$\boldsymbol{l} \equiv (\cos\varphi, \sin\varphi, 0), \tag{9}$$

$$\boldsymbol{E} \equiv (\cos\psi, \sin\psi, 0). \tag{10}$$

The relationship between the opto-magnetic torques in tensorial notation found in ref. 35 and the trigonometric representation based on the φ, ψ angles is detailed in Table 1. First of all, it is easy to see that given the $\theta_e = \pi/2$ condition, tensors 3 and 9 become null in our geometry since ϵ_{z,z^*} are zero. Secondly, it is worth pointing out that tensors 4 and 24 are linked via $\pm\pi/4$ rotations with respect to φ and ψ. As such, if we set $\psi = 45°$ to maximise the magnitude of tensor 24, tensor 4 becomes zero. Finally, the spatial variation of tensor 24 can be written in a compact form as:

$$T_z = A\cos(2\varphi)\sin(2\psi), \tag{11}$$

where we insert the proportionality factor A in units of Tesla to recover Eq. (1) in the main text. As presented in Fig. 2 of ref. 35, for a typical laser intensity of $I = 10$ GW/cm^2, photon energy of $\nu = 1.55$ eV and $\Gamma = 25$ meV, A evaluates to 12 yJ/μ_s or approximately 0.346 T.

Data availability

The data supporting the findings of this study are available from the corresponding author upon reasonable request.

Received: 8 November 2024; Accepted: 4 February 2025;
Published online: 28 March 2025

References

1. Jungwirth, T., Marti, X., Wadley, P. & Wunderlich, J. Antiferromagnetic spintronics. *Nat. Nanotechnol.* **11**, 231–241 (2016).
2. Baltz, V. et al. Antiferromagnetic spintronics. *Rev. Mod. Phys.* **90**, 015005 (2018).
3. Parkin, S. S., Hayashi, M. & Thomas, L. Magnetic domain-wall racetrack memory. *Science* **320**, 190–194 (2008).
4. Yang, S. H., Ryu, K. S. & Parkin, S. Domain-wall velocities of up to 750 m/s^{-1} driven by exchange-coupling torque in synthetic antiferromagnets. *Nat. Nanotechnol.* **10**, 221–226 (2015).
5. Allwood, D. A. et al. Magnetic domain-wall logic. *Science* **309**, 1688–1692 (2005).
6. Lan, J., Yu, W. & Xiao, J. Antiferromagnetic domain wall as spin wave polarizer and retarder. *Nat. Commun.* **8**, 1–7 (2017).
7. Hedrich, N. et al. Nanoscale mechanics of antiferromagnetic domain walls. *Nat. Phys.* **17**, 574–577 (2021).
8. Zhang, S. & Tserkovnyak, Y. Antiferromagnet-based neuromorphics using dynamics of topological charges. *Phys. Rev. Lett.* **125**, 207202 (2020).
9. Ababei, R. V. et al. Neuromorphic computation with a single magnetic domain wall. *Sci. Rep.* **11**, 1–13 (2021).
10. Otxoa, R. M., Tatara, G., Roy, P. E. & Chubykalo-Fesenko, O. Tailoring elastic and inelastic collisions of relativistic antiferromagnetic domain walls. *Sci. Rep.* **13**, 21153 (2023).
11. Schryer, N. L. & Walker, L. R. The motion of 180° domain walls in uniform dc magnetic fields. *J. Appl. Phys.* **45**, 5406–5421 (1974).
12. Tatara, G. & Kohno, H. Theory of current-driven domain wall motion: spin transfer versus momentum transfer. *Phys. Rev. Lett.* **92**, 086601 (2004).
13. Hinzke, D. & Nowak, U. Domain wall motion by the magnonic spin seebeck effect. *Phys. Rev. Lett.* **107**, 027205 (2011).
14. Akhmediev, N. & Karlsson, M. Cherenkov radiation emitted by solitons in optical fibers. *Phys. Rev. A* **51**, 2602 (1995).
15. Yan, M., Kákay, A., Andreas, C. & Hertel, R. Spin-Cherenkov effect and magnonic Mach cones. *Phys. Rev. B Condens. Matter Mater. Phys.* **88**, 220412 (2013).
16. Gomonay, O., Jungwirth, T. & Sinova, J. High antiferromagnetic domain wall velocity induced by Néel spin-orbit torques. *Phys. Rev. Lett.* **117**, 017202 (2016).
17. Otxoa, R. M. et al. Walker-like domain wall breakdown in layered antiferromagnets driven by staggered spin-orbit fields. *Commun. Phys.* **3**, 1–9 (2020).
18. Železný, J. et al. Relativistic néel-order fields induced by electrical current in antiferromagnets. *Phys. Rev. Lett.* **113**, 157201 (2014).
19. Wadley, P. et al. Spintronics: electrical switching of an antiferromagnet. *Science* **351**, 587–590 (2016).
20. Roy, P. E., Otxoa, R. M. & Wunderlich, J. Robust picosecond writing of a layered antiferromagnet by staggered spin-orbit fields. *Phys. Rev. B* **94**, 014439 (2016).
21. Bodnar, S. Y. et al. Writing and reading antiferromagnetic Mn2Au by Néel spin-orbit torques and large anisotropic magnetoresistance. *Nat. Commun.* **9**, 1–7 (2018).
22. Olejník, K. et al. Terahertz electrical writing speed in an antiferromagnetic memory. *Sci. Adv.* https://www.science.org/doi/10.1126/sciadv.aar3566 (2018).
23. Godinho, J. et al. Electrically induced and detected Néel vector reversal in a collinear antiferromagnet. *Nat. Commun.* **9**, 1–8 (2018).
24. Otxoa, R. M., Atxitia, U., Roy, P. E. & Chubykalo-Fesenko, O. Giant localised spin-Peltier effect due to ultrafast domain wall motion in antiferromagnetic metals. *Commun. Phys.* **3**, 1–7 (2020).
25. Janda, T. et al. Magneto-Seebeck microscopy of domain switching in collinear antiferromagnet CuMnAs. *Phys. Rev. Mater.* **4**, 094413 (2020).
26. Kimel, A. V. & Li, M. Writing magnetic memory with ultrashort light pulses. *Nat. Rev. Mater.* **4**, 189–200 (2019).
27. Kimel, A. V., Kirilyuk, A., Tsvetkov, A., Pisarev, R. V. & Rasing, T. Laser-induced ultrafast spin reorientation in the antiferromagnet TmFeO3. *Nature* **429**, 850–853 (2004).
28. Kampfrath, T. et al. Coherent terahertz control of antiferromagnetic spin waves. *Nat. Photonics* **5**, 31–34 (2010).
29. Wienholdt, S., Hinzke, D. & Nowak, U. THz switching of antiferromagnets and ferrimagnets. *Phys. Rev. Lett.* **108**, 247207 (2012).
30. Disa, A. S. et al. Polarizing an antiferromagnet by optical engineering of the crystal field. *Nat. Phys.* **16**, 937–941 (2020).
31. Dannegger, T. et al. Ultrafast coherent all-optical switching of an antiferromagnet with the inverse Faraday effect. *Phys. Rev. B* **104**, L060413 (2021).
32. Grigorev, V. et al. Optically triggered Néel vector manipulation of a metallic antiferromagnet Mn2Au under strain. *ACS Nano* **16**, 20589–20597 (2022).
33. Weißenhofer, M., Foggetti, F., Nowak, U. & Oppeneer, P. M. Néel vector switching and terahertz spin-wave excitation in Mn2Au due to femtosecond spin-transfer torques. *Phys. Rev. B* **107**, 174424 (2023).
34. Behovits, Y. et al. Terahertz Néel spin-orbit torques drive nonlinear magnon dynamics in antiferromagnetic Mn2Au. *Nat. Commun.* **14**, 1–10 (2023).
35. Freimuth, F., Blügel, S. & Mokrousov, Y. Laser-induced torques in metallic antiferromagnets. *Phys. Rev. B* **103**, 174429 (2021).
36. Merte, M. et al. Photocurrents, inverse Faraday effect, and photospin Hall effect in Mn2Au. *APL Mater.* **11**, 71106 (2023).
37. Freimuth, F., Blügel, S. & Mokrousov, Y. Laser-induced torques in metallic ferromagnets. *Phys. Rev. B* **94**, 144432 (2016).
38. Němec, P. et al. Experimental observation of the optical spin transfer torque. *Nat. Phys.* **8**, 411–415 (2012).
39. Ramsay, A. J. et al. Optical spin-transfer-torque-driven domain-wall motion in a ferromagnetic semiconductor. *Phys. Rev. Lett.* **114**, 067202 (2015).
40. Kimel, A. V. et al. Ultrafast non-thermal control of magnetization by instantaneous photomagnetic pulses. *Nature* **435**, 655–657 (2005).
41. Quessab, Y. et al. Helicity-dependent all-optical domain wall motion in ferromagnetic thin films. *Phys. Rev. B* **97**, 054419 (2018).
42. Ross, J. L. et al. Ultrafast antiferromagnetic switching of mn2au with laser-induced optical torques. *npj Comput. Mater.* **10**, 234 (2024).
43. Evans, R. F. et al. Atomistic spin model simulations of magnetic nanomaterials. *J. Phys. Condens. Matter* **26**, 103202 (2014).
44. Baryakhtar, I. & Ivanov, B. Effective equation of motion for an antiferromagnet in weak magnetic fields. *Fiz. Nizk. Temp.* **5**, 361 (1979).
45. Baryakhtar, I. & Ivanov, B. Nonlinear waves in antiferromagnets. *Solid State Commun.* **34**, 545 (1980).
46. Ivanov, B. A. & Kolezhuk, A. K. Solitons with internal degrees of freedom in 1d Heisenberg antiferromagnets. *Phys. Rev. Lett.* **74**, 1859–1862 (1995).
47. Papanicolaou, N. Antiferromagnetic domain walls. *Phys. Rev. B* **51**, 15062–15073 (1995).
48. Rama-Eiroa, R. et al. Inertial domain wall characterization in layered multisublattice antiferromagnets. *J. Magn. Magn. Mater.* **560**, 169566 (2022).
49. Sapozhnik, A. A. et al. Direct imaging of antiferromagnetic domains in mn2au manipulated by high magnetic fields. *Phys. Rev. B* **97**, 134429 (2018).
50. Khmelevskyi, S. & Mohn, P. Layered antiferromagnetism with high Neel temperature in the intermetallic compound Mn2 Au. *Appl. Phys. Lett.* **93**, 162503 (2008).
51. Shick, A. B., Khmelevskyi, S., Mryasov, O. N., Wunderlich, J. & Jungwirth, T. Spin-orbit coupling induced anisotropy effects in bimetallic antiferromagnets: a route towards antiferromagnetic

spintronics. *Phys. Rev. B Condens. Matter Mater. Phys.* **81**, 212409 (2010).
52. Stroh, A. N. Steady state problems in anisotropic elasticity. *J. Math. Phys.* **41**, 77–103 (1962).
53. One-dimensional dislocations. I. Static theory. *Proceedings of the Royal Society of London. Series A. Mathematical and Physical Sciences* **198**, 205–216 (1949).
54. Parlak, U., Adam, R., Bürgler, D. E., Gang, S. & Schneider, C. M. Optically induced magnetization reversal in [Co/Pt]N multilayers: role of domain wall dynamics. *Phys. Rev. B* **98**, 214443 (2018).
55. Wolba, B., Gomonay, O. & Kravchuk, V. P. Chaotic antiferromagnetic nano-oscillator driven by spin torque. *Phys. Rev. B* **104**, 024407 (2021).
56. Ovcharov, R., Galkina, E., Ivanov, B. & Khymyn, R. Spin hall nano-oscillator based on an antiferromagnetic domain wall. *Phys. Rev. Appl.* **18**, 024047 (2022).
57. Kurenkov, A., Fukami, S. & Ohno, H. Neuromorphic computing with antiferromagnetic spintronics. *J. Appl. Phys.* **128**, 10902 (2020).
58. Godinho, J. et al. Antiferromagnetic domain wall memory with neuromorphic functionality. *npj Spintron.* **2**, 39 (2024).
59. Bourianoff, G., Pinna, D., Sitte, M. & Everschor-Sitte, K. Potential implementation of reservoir computing models based on magnetic skyrmions. *AIP Adv.* **8**, 55602 (2018).
60. Bar'yakhtar, V. G., Ivanov, B. A. & Chetkin, M. V. Dynamics of domain walls in weak ferromagnets. *Usp. Fiz. Nauk* **146**, 417–458 (1985).
61. Šmejkal, L., Sinova, J. & Jungwirth, T. Emerging research landscape of altermagnetism. *Phys. Rev. X* **12**, 040501 (2022).

Acknowledgements

This project has received funding from the European Union's Horizon 2020 research and innovation programme under the Marie Skłodowska-Curie International Training Network COMRAD, grant agreement No 861300. The atomistic simulations were undertaken on the VIKING cluster, which is a high-performance computing facility provided by the University of York. F.F. and Y.M. acknowledge the funding by the Deutsche Forschungsgemeinschaft (DFG, German Research Foundation) – TRR 173/2 – 268565370 (project A11) and Sino-German research project DISTOMAT (MO 1731/10-1). The work of O.C.-F. has been supported by DFG via CRC/TRR 227, project ID 328545488 (Project MF).

Author contributions

P.-I.G., J.L.R. and R.M.O. conceived the idea and designed the study. J.L.R. and P.-I.G. carried out the atomistic spin dynamics simulations. F.F. and Y.M. facilitated the understanding and implementation of the ab initio calculated optical torques in the atomistic spin model. R.F.L.E. and R.C. provided invaluable input in the interpretation of the atomistic spin dynamics results. P.-I.G., J.L.R, O.C.-F. and R.M.O. developed the theoretical framework. P.-I.G. and O.C.-F. wrote the initial draft and P.-I.G. prepared the figures. All authors reviewed the manuscript and provided comments and/or edited the final version of the draft.

Competing interests

The authors declare no competing interests.

Additional information

Supplementary information The online version contains supplementary material available at https://doi.org/10.1038/s44306-025-00075-2.

Correspondence and requests for materials should be addressed to Paul-Iulian Gavriloaea or Rubén M. Otxoa.